Photoelectron angular distributions of low-order above-threshold ionization of Xe in the multiphoton regime

Min Li, Yunquan Liu,[*] Hong Liu, Yudong Yang, Jialei Yuan, Xianrong Liu, Yongkai Deng, Chengyin Wu, and Qihuang Gong

State Key Lab for Mesoscopic Physics, School of Physics, Peking University, Beijing 100871, People's Republic of China

We present high-resolution two-dimensional momentum distributions and energy-angular distributions of photoelectrons from xenon atoms, ionized by an 800-nm, 25-fs linearly polarized laser at intensities of $(1.8$–$4.4) \times 10^{13}$ W/cm^2. The angular distributions of low-energy photoelectrons exhibit pronounced intensity-dependent features. The photoelectron angular distributions (PADs) of nonresonant ionization, Freeman resonance, and main order above-threshold ionization at different laser intensities are analyzed. We have characterized the PADs of above-threshold ionization up to the fourth order and have confirmed the angular momentum selection rule of $\Delta l = 1$ for above-threshold ionization at all laser intensities. We observe that the channel of nine-photon resonant ionization has switched to a ten-photon process but nine-photon nonresonance still remains for xenon.

PACS number(s): 32.80.Fb, 32.80.Rm

I. INTRODUCTION

Above-threshold ionization (ATI), since its discovery three decades ago, has been one of the most intriguing phenomena in the area of strong-field atomic physics [1–4]. In this process, an electron can absorb S ($S \geqslant 0$) photons, i.e., the ATI order, in excess of N, the minimum number necessary to overcome the ionization potential. Therefore, ATI manifests itself as the regular peaks separated by one photon in the energy spectrum. Due to resonantly enhanced multiphoton ionization, the low-order ATI peaks can break up into substructures in the short pulse limit, which is called Freeman resonance [5]. Because of electron ponderomotive motion, the atom can be excited to an ac-Stark-shifted Rydberg state by an integer number of photons, and then be ionized by an additional one or more photons into the continuum.

A relatively intuitive way to study the ATI process is to measure and to analyze the photoelectron angular distributions (PADs). Initially, the PADs of ATI peaks were measured more than ten years ago by the time-of-flight spectrometer via rotating the laser polarization direction. Yang *et al.* [6] observed a ring structure in the PADs of high-order ATI peaks. Nandor *et al.* [7] found that the PADs of low-order ATI peaks are constructed by main lobe, jets, and wings. They suggested that the amount of the jet structures corresponds to the angular momentum of the resonant Rydberg state. Theoretically, Guo *et al.* [8] established a scaling law for PADs and they found that the number of jets can be determined by the maxima of generalized phased Bessel functions. They predicted that under certain conditions three more jets may appear with only one-more-photon absorption. In consideration of the long-range Coulomb potential, Chen *et al.* [9] theoretically studied that the low-energy electrons exhibit pronounced fanlike structures that agreed well with the experimental observation of Rudenko *et al.* [10] and Maharjan *et al.* [11]. Chen *et al.* [9] further established an empirical rule that the dominant angular momentum of the low-energy photoelectrons is only determined by the initial state and the minimum number of photons needed to ionize the atoms. An

alternative interpretation of this dominant angular momentum was reported by Arbó *et al.* [12], who attributed this to being the natural result of interfering paths under the combined effect of the Coulomb potential and the laser field. This interpretation was confirmed experimentally by Marchenko *et al.* [13], and two major contributions arising from the interference as well as from Freeman resonance can be distinguished from the momentum spectra in their experiment. Their subsequent work [14] showed that the presence of nonresonant ionization could influence the resonant substructures in the energy spectrum.

In this paper, we present two-dimensional momentum distributions and energy-angular distributions of photoelectrons from xenon atoms at different laser intensities measured by a cold-target recoil ion momentum spectroscopy (COLTRIMS) spectrometer (see Ref. [15] for reviews). COLTRIMS is a very powerful tool to study laser-matter interaction, which can provide full-differential data compared with other time-of-flight instruments used before. Benefitting from this advantage, we have precisely measured the PADs of above-threshold ionization of Xe to have deep insight into each order ATI peak and to test the available theories [8,9,12]. The PADs of the low-order ATI peaks reveal that they are dominated by a certain angular momentum. The dominant angular momentum could help us understand the ionization process and find the transition selection rule. The paper is organized as follows. In Sec. II, the experimental setup is briefly described. Section III gives our main results and discussions. We have compared our experimental results with the available results based on nonperturbative scattering theory by Guo *et al.* [8]. The conclusion is made in Sec. IV.

II. EXPERIMENTAL SETUP

The experimental setup is composed of a COLTRIMS system and an amplified femtosecond Ti:sapphire laser system. Full details of the COLTRIMS system are described elsewhere [16]. Briefly, the xenon atoms at high pressure are forced through a nozzle into vacuum. A cone-shaped skimmer of a 290 μm diameter is placed behind the nozzle to extract the cooled beam. After the collimation by two pinholes, the geometrically well-shaped atomic beam is restricted to

_____

[*]yunquan.liu@pku.edu.cn

interact with a focused laser pulse. The spectrometer is divided into acceleration and drift regions for ions and electrons. The ionized ions and electrons are collected by ~ 3 V/cm electric field and ~ 8 G magnetic field, which allow us to collect the electrons with the maximum transverse momentum up to 1.2 a.u. with a 4π solid angle. Multichannel plate layers combined with the delay-line-anode detectors are used to record time-of-flights and positions of the electrons and ions, and to realize the measurement of the three-dimensional momentum of all fragments. With that, we can have the total energy of photoelectrons as well as the PADs of above-threshold ionization. The pressure below 1×10^{-10} mbar can be achieved in the main COLTRIMS chamber.

The laser system can produce a 25-fs linearly polarized pulse, at a center wavelength of 800 nm (photon energy ~ 1.55 eV) up to 2.5 W with 3-kHz repetition rate. The laser spectral width is ~ 30 nm. The laser beam is focused onto the supersonic xenon gas jet by a 75-mm focal length silver-plated mirror, mounted on a five-dimensional driver. The laser peak intensity is calibrated by measuring the beginning of the plateau in the single-ionized photoelectron energy spectrum, whose position is $\sim 2U_p$ in theory [17], where U_p is the ponderomotive potential (the cycle-averaged quiver energy of a free electron in the laser field). We estimate that the uncertainty of the calibrated laser intensity is no more than $\pm 10\%$.

III. RESULTS AND DISCUSSIONS

We first show the angle-integrated energy spectra in Fig. 1. The neighboring ATI peaks are separated by one-photon energy. In Fig. 1, the peaks labeled by simple arabic numerals are the main ATI peaks [for example, "1" indicates the first ATI peaks ($S = 0$) and so on]. The peaks labeled as "$4f$" and "$5g$" are Freeman resonance via the corresponding states. Other peaks with low energy mainly come from nonresonant ionization.
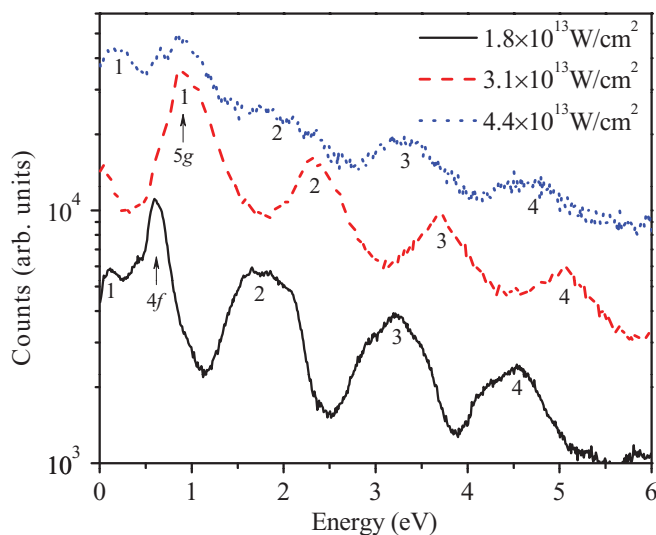

FIG. 1. (Color online) Angle-integrated energy spectra at three different peak intensities. The vertical coordinate is logarithmic. The purely arabic numerals indicate the ATI order and the "$4f$" and "$5g$" indicate the corresponding resonant Rydberg states. The data of the dashed (dotted) line have been shifted up by a factor of 4 (20).
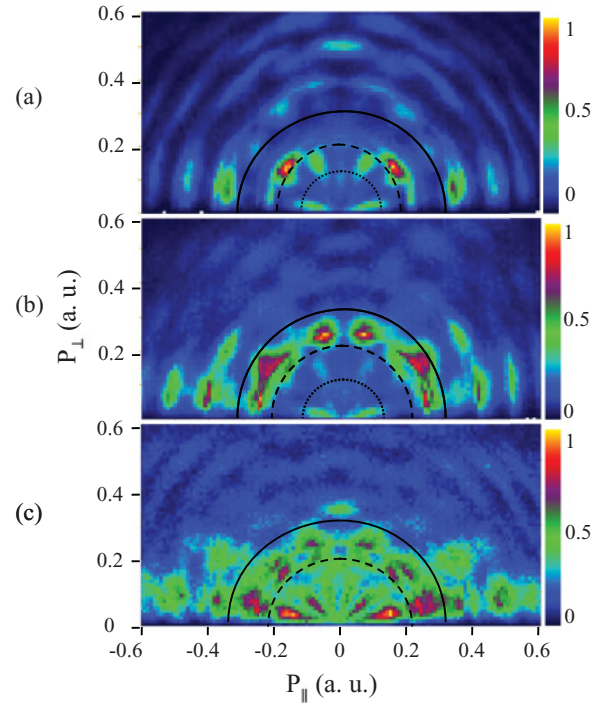

FIG. 2. (Color online) Density plot of two-dimensional photoelectron momentum distributions at (a) 1.8×10^{13} W/cm^2; (b) 3.1×10^{13} W/cm^2; (c) 4.4×10^{13} W/cm^2, respectively. The abscissa $P_{\parallel}$ is the momentum parallel to the polarization direction and the vertical coordinate $P_{\perp}$ is the momentum perpendicular to that direction. The solid lines and the abscissas limit the energy region lower than one photon. Two (or three at 1.8×10^{13} and 3.1×10^{13} W/cm^2) regions divided by the dashed (and dotted) line can be easily distinguished by the different angular distributions.

In order to explore the evolution of each peak in the energy spectra with the laser intensity, two-dimensional momentum distributions and energy-angular distributions of photoelectrons are presented in Figs. 2 and 3, respectively. The low-energy photoelectrons show pronounced intensity-dependent structures. In Fig. 2, the solid lines and the abscissas limit the photoelectrons with energy lower than one photon. In this energy range, the photoelectrons arising from interference (below the dashed lines with fanlike patterns) and from Freeman resonance (between dashed lines and solid lines with ringlike patterns) can be fairly distinguished. Comparing with Fig. 1, we can find that the ringlike patterns do not completely correspond to the main ATI peaks. We will individually analyze the angular distributions of nonresonance, Freeman resonance, and each order ATI peak for three intensities in detail.

A. Angular distributions of near-threshold photoelectrons

The near-threshold photoelectrons denote the fanlike patterns below the dashed lines in Fig. 2 (whose energy is less than 0.5 eV). The PADs of the fanlike patterns at an intensity of 3.1×10^{13} W/cm^2 are similar to those at 1.8×10^{13} W/cm^2 as seen in Figs. 2(a) and 2(b). We observe an evident intensity-dependent feature that there are two parts of photoelectrons with different angular distributions at intensities of both 1.8×10^{13} and 3.1×10^{13} W/cm^2 (their energy is 0–0.3 eV
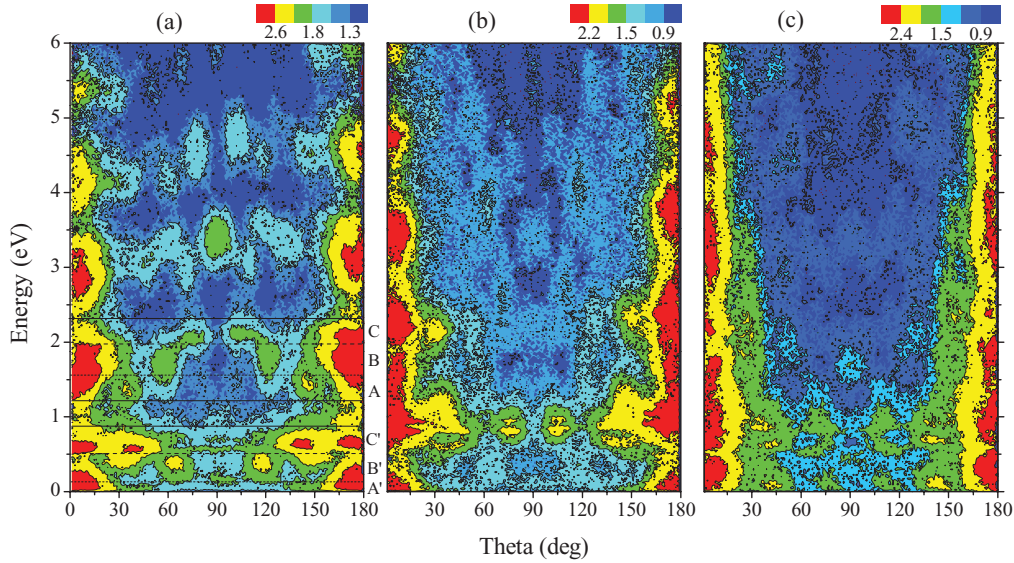
FIG. 3. (Color online) Density plots of two-dimensional energy-angular distributions at (a) 1.8×10^{13} W/cm^2; (b) 3.1×10^{13} W/cm^2; (c) 4.4×10^{13} W/cm^2, respectively. The abscissa is theta (θ), the angle between electrons emitted and laser polarization direction; the vertical coordinate is the photoelectron kinetic energy; the color represents the counts on the logarithmic scale. The A, B, and C regions are one-more-photon absorption from the A', B', and C' regions, respectively, which correspond to the three regions lower than one-photon energy in Fig. 2(a).

and 0.3–0.5 eV respectively), whereas photoelectrons with exclusive angular distributions are found fanning out radially from the origin at 4.4×10^{13} W/cm^2. The photoelectrons with energy of 0–0.3 eV and 0.3–0.5 eV will be studied separately at 1.8×10^{13} and 3.1×10^{13} W/cm^2.

The angular differential distributions of near-threshold photoelectrons are illustrated in Fig. 4. The angular differential probability shows pronounced jet structures that resemble those of the square of a single Legendre polynomial $[P_l(\cos\theta)]^2$ of degree l, which represents the dominant

FIG. 4. (Color online) Polar plots of the PADs of near-threshold photoelectrons at (a) 1.8×10^{13} W/cm^2 with energy lower than 0.3 eV; (b) 1.8×10^{13} W/cm^2 with energy of 0.3–0.5 eV; (c) 4.4×10^{13} W/cm^2 with energy lower than 0.5 eV. The squares are the experimental data, and the red solid lines are $[P_4(\cos\theta)]^2$, $[P_6(\cos\theta)]^2$, and $[P_5(\cos\theta)]^2$, respectively. All the lines are symmetric.

angular momentum of these electrons. Therefore, the angular differential probability can be expressed [18]:

$$\frac{d^2 P}{dEd(\cos\theta)} \approx [P_l(\cos\theta)]^2, \qquad (1)$$

Here, E is the photoelectron energy. We assume the magnetic quantum number m is a constant ($m = 0$). The fitted distributions are in good agreement with the experimental data except for the yield intensity. The deviation in the vicinity of $0°$ and $180°$ is due to the data analysis. In the data processing, since we construct the energy-angular distributions from the three-dimensional momentum vector, it will introduce this error when transferring from the laboratory coordinate to the polar coordinate.

The dominant angular momentum is concerned with the transient state of ionization. First we analyze the resonant intermediate state of near-threshold photoelectrons with energy lower than 0.3 eV at 1.8×10^{13} and 3.1×10^{13} W/cm^2 and lower than 0.5 eV at 4.4×10^{13} W/cm^2. The atom at an intermediate state will absorb an additional photon to continuum if the multiphoton process occurs. Therefore, the binding energy of the resonant state can be calculated through the measured electron energy minus one photon. Then we can learn the angular momentum of the transient resonant states at three laser intensities. The dominant angular momentum of near-threshold photoelectrons at three intensities is 4, 4, and 5, as shown in Figs. 4(a) and 4(c), which reveal that they come from f, f, and g states, respectively. However, when comparing with the available atomic database [19], we cannot find any state that satisfies the angular momentum in that energy level region even considering the laser spectral property. Thereby, the near-threshold photoelectrons may come from the nonresonant ionization process.

We find an evident difference of the jet positions and heights between the fitted distributions and the experimental
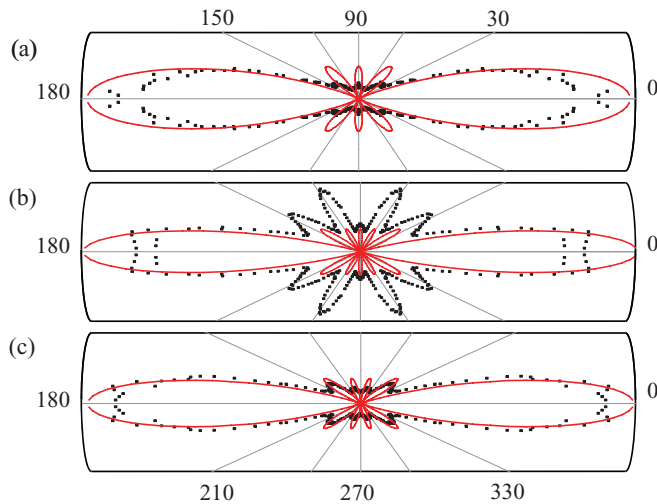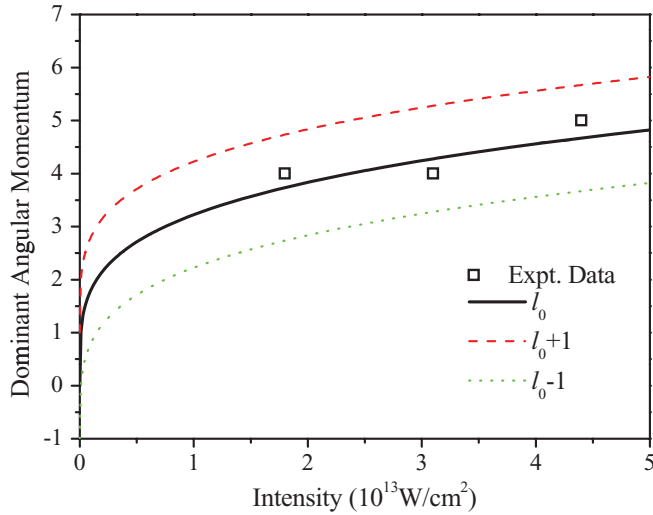
FIG. 5. (Color online) Dominant angular momentum of near-threshold photoelectrons as a function of laser intensity. The squares are the dominant angular momentum of photoelectrons with energy lower than 0.3 eV at 1.8×10^{13} and 3.1×10^{13} W/cm^2 and lower than 0.5 eV at 4.4×10^{13} W/cm^2 from the experimental data. The black solid line is the semiclassical result. The dashed red and dotted green lines restrict the uncertainty region due to quantum discreteness.

data as shown in Fig. 4. Three factors may be responsible for this difference. First, the single Legendre polynomial is just a single partial wave for the angular distribution. The jet number only points out that the PADs are dominated by one certain angular momentum, but other partial waves may also contribute. The nonresonant ionization leads to many partial waves with different angular momentum. These partial waves, unless negligible, have an influence on the PADs, but we ignore other partial waves in the fitted distributions. Second, the PADs are also affected by the overlap between two or more adjacent peaks. The electrons are taken out from a definite energy interval, but not from a complete peak. As a result, the electrons from the adjacent states may be included. Third, the detection efficiency of different angles is not absolutely the same and could lead to the inaccuracy of the statistics.

From the theoretical perspective, Arbó *et al.* proposed an interpretation that the angular distributions of near-threshold photoelectrons are due to the interference between different trajectories of the continuum photoelectrons in the laser field as well as the Coulomb potential of the parent ion [12], via classical-trajectory Monte-Carlo calculations. The dominant angular momentum of near-threshold electrons was obtained with the analytical formula in atomic units [12,13]:

$$l_0 = (2Z_T \alpha)^{1/2}, \qquad (2)$$

where l_0 is the dominant classical angular momentum, Z_T is the remaining charge of the atom after ionization, and $\alpha = F_0/\omega^2$ is the electron quiver amplitude in laser field with the amplitude F_0 and the frequency ω. This equation is valid if the uncertainty $l_0 \pm 1$ due to quantum discreteness is considered. The angular momentum of near-threshold photoelectrons, measured in the experiment as well as predicted by the semiclassical theory, is shown in Fig. 5. The theoretical results agree with our experimental data very well. Consequently, the

near-threshold photoelectrons can be treated as a nonresonant process via a result of interfering paths under the combined effect of the Coulomb potential and the laser field, which has been confirmed in a recent lithium experiment [20].

Now we study the photoelectrons with the energy of 0.3–0.5 eV between the dotted and dashed lines in Figs. 2(a) and 2(b). These photoelectrons have different angular distributions with those of photoelectrons with energy lower than 0.3 eV as shown in Fig. 4(b). The fanlike patterns, at first glance, indicate the nonresonant ionization and there are no states to be assigned to these electrons satisfying the angular momentum $l = 6$ when we compare with the atomic database [19]. The angular momentum also violates the semiclassical theory by Arbó *et al.* We believe another channel might be responsible for these electrons. This structure may come from the ac Stark splitting, i.e., a similar mechanism that is proposed by Wiehle *et al.* [21] for Argon, via one-photon coupling between the $5d$ and $4f$ states. This coupling will be forbidden due to channel closing [22] when the intensity increases to 4.4×10^{13} W/cm^2, since seven photons are not enough to excite the ac-Stark-shifted $5d$ state. Just as in [21], the angular momentum of this dressed transition performs surprisingly two more than the expected, which indicates that the transient process of ionization plays a key role to the PADs.

On the other hand, the comparatively large difference between experimental data and fitted distributions of the dressed transition in Fig. 4(b) may come from the effect of the overlap with other photoelectrons, which implies that the angular momentum $l = 6$ may not be absolutely correct. Intuitively, the angular distributions (between the dotted and dashed lines in Fig. 2) are just similar with the density distributions of the d-shell electron cloud ($l = 2$, $m = \pm 1$). With the binding energy, we extrapolate that $7p$-resonant ionization might also contribute to these photoelectrons.

B. Angular distributions of Freeman resonance structure

The ringlike patterns with energy of $0.5 \sim 1.55$ eV between the dashed and solid lines in Fig. 2 come from Freeman resonance. The angular distributions of Freeman resonance at three intensities are shown in Fig. 6. From the dominant angular momentum and the binding energy, we can infer the resonant Rydberg state. At 1.8×10^{13} W/cm^2, the dominant angular momentum of the Freeman resonance is 4 in Fig. 6(a). With the binding energy, we can know that the intermediate state matches the $4f$ state (the peak labeled $4f$ in Fig. 1). At 3.1×10^{13} and 4.4×10^{13} W/cm^2, the angular distributions of the Freeman resonance are shown in Figs. 6(b) and 6(c), respectively. The angular momentum for both is 5, and their binding energy agrees quite well with the $5g$ Rydberg state.

We observe another pronounced intensity-dependent feature of the resonant structure, e.g., there is a single peak at an intensity of 1.8×10^{13} W/cm^2, while two subpeaks with the same angular distributions appear at 3.1×10^{13} and 4.4×10^{13} W/cm^2. This splitting effect, also observed in our previous experiment [23], is much more distinct as the intensity increases. Increasing the laser intensity from 1.8×10^{13} to 3.1×10^{13} W/cm^2, the nine-photon channel has switched to a ten-photon channel. This is the channel-switching effect [22]. Considering the ponderomotive effect and the parity
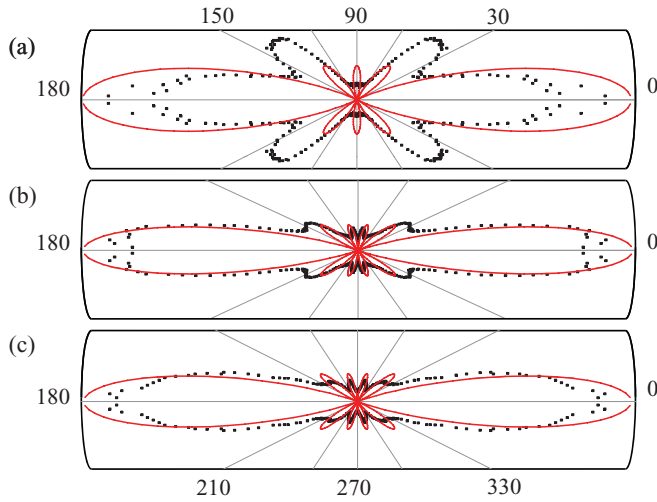
FIG. 6. (Color online) Polar plots of the PADs of Freeman resonance with energy of 0.5–1.55 eV at (a) 1.8×10^{13} W/cm^2; (b) 3.1×10^{13} W/cm^2; (c) 4.4×10^{13} W/cm^2. The squares are the experimental data and the red solid lines are $[P_4(\cos\theta)]^2$, $[P_5(\cos\theta)]^2$, and $[P_5(\cos\theta)]^2$, respectively. All the lines are symmetric.

selection rule, we can learn that these peaks correspond to a nine-, ten-, and ten-photon process, respectively, at intensities from 1.8×10^{13} to 4.4×10^{13} W/cm^2. The ac-Stark-shifted $4f$ state will enhance the ionization via resonance with eight photons at 1.8×10^{13} W/cm^2, but at higher intensities one more photon is absorbed and the resonant state will switch to the $5g$ state. Other excited states might also be resonant only if their nonlinear ionization rate and the relative oscillator strength are large enough [5]. The ac-Stark-shifted $5g$ and $6g$ states may be resonant with nine-photon absorption simultaneously due to the slight energy difference between them, giving rise to the splitting of the Freeman resonance.

Further, at 3.1×10^{13} W/cm^2, the nonresonant peak (with energy lower than 0.3 eV) in Fig. 1 corresponds to a nine-photon process, whereas the Freeman resonance (with energy of 0.3–0.5 eV) is a ten-photon process. That is, though the channel of nine-photon resonant ionization has closed, the nine-photon nonresonance still remains. As far as we know, this phenomenon of the channel partially closing has not been reported. The $4f$ and high-lying Rydberg g state could be simultaneously resonant with eight and nine photons at a certain laser intensity [24], which is nevertheless not observed in our experiment. Moreover, the low-energy peaks in the spectrum will shift downward and then disappear with the increase of the laser intensity. As a result, when the laser intensity increases to about 3.6×10^{13} W/cm^2, the nine-photon channel will close eventually.

C. Angular distributions of above-threshold ionization and selection rule

We show the angular distributions of the first main ATI peaks in Figs. 4(a), 6(b), and 4(c) at three intensities of 1.8×10^{13}, 3.1×10^{13}, and 4.4×10^{13} W/cm^2, respectively. All the PADs show the main lobe, jets, and wings. The dominant angular momenta of the first ATI peaks at 1.8×10^{13}, 3.1×10^{13}, and 4.4×10^{13} W/cm^2 are 4, 5, and 5,
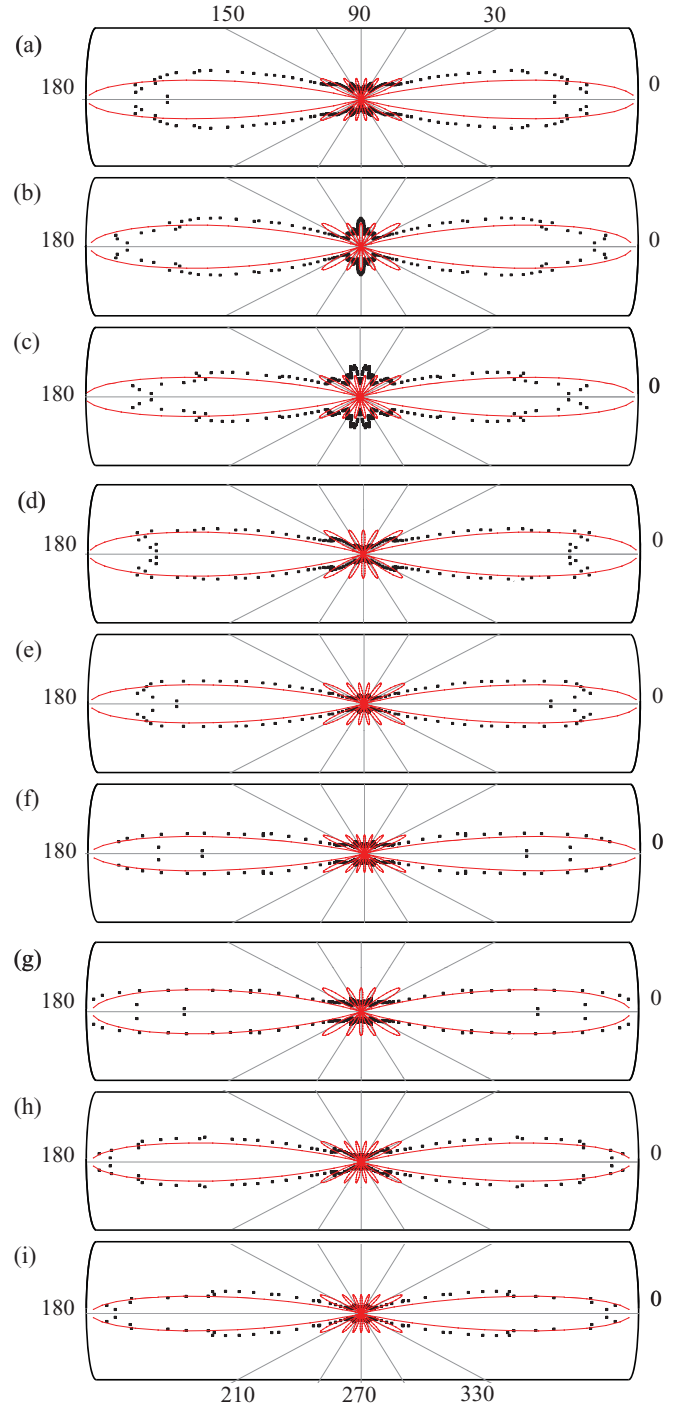

FIG. 7. (Color online) Polar plots of the PADs of the second, third, and fourth ATI peaks at intensities of (a–c) 1.8×10^{13} W/cm^2; (d–f) 3.1×10^{13} W/cm^2; (g–i) 4.4×10^{13} W/cm^2, respectively. The squares are the experimental data and the red solid lines are $[P_l(\cos\theta)]^2$, where l is (a–c) 7, 6, 7; (d–f) 6, 7, 8; and (g–i) 6, 7, 8, respectively. All the lines are symmetric.

respectively. The angular distributions of other order up to fourth ATI peaks at three intensities are showed in Fig. 7. The dominant angular momenta of the first- to fourth-order ATI peaks are 4, 7, 6, and 7, respectively, at 1.8×10^{13} and are 5, 6, 7, and 8, respectively, at 3.1×10^{13} and 4.4×10^{13} W/cm^2.

Thus, the selection rule for the dominant angular momentum of the main ATI peaks can be confirmed by

$$\Delta l = 1. \tag{3}$$

Here Δl is the angular momentum of a specific ATI peak minus that of the previous one. The result illustrates the success of the dipolar selection rule in multiphoton ionization. One more photon is absorbed as the ATI order increases by one. If the angular momentum of a certain ATI peak is l and the dipolar selection rule is obeyed, the angular momentum of the next ATI peak will be $l + 1$ or $l - 1$. Chen *et al.* [9] predicted that the dipole transition matrix element from l to $l + 1$ is larger than for the transition from l to $l - 1$. Therefore, the partial wave $l + 1$ will hide the contributions of the partial wave $l - 1$ and the PADs of the next ATI peak will be dominated by $l + 1$.

In our experiment, the dominant angular momentum of the ATI peaks steps up one by one with increasing the ATI order, except for the second ATI peak at 1.8×10^{13} W/cm^2. Now, we pay attention to this "abnormal" ATI peak. In Fig. 1, we can see that this peak is much broader than the others, and two-dimensional energy-angular distributions reveal that the peak contains three regions which are labeled A, B, and C in Fig. 3(a). In fact, the three regions correspond to one-more-photon absorption than the first main ATI, the $5d$-$4f$ dressed transition, and Freeman resonance via $4f$ state respectively [labeled as A', B', and C' in Fig. 3(a)]. The PADs of the three regions (A, B, and C) overlap with each other and thus are difficult to extract differentially. If the dipolar selection rule is obeyed, the dominant angular momenta of A, B, and C regions are 5, 7, and 5, respectively. The angular distributions of this ATI peak would exhibit $l = 7$ as a whole because the large angular momentum will hide the small one. If we rule out the influence of the overlap, the second main ATI peak at 1.8×10^{13} W/cm^2 will show the actual dominant angular momentum $l = 5$.

We can observe in Fig. 1 that the second ATI peak at 4.4×10^{13} W/cm^2 exhibits a similar broad peak, which also contains three regions corresponding to one-more-photon absorption than the first main ATI and the Freeman resonance via the $5g$ and $6g$ states, respectively. Unlike at 1.8×10^{13} W/cm^2, the angular distributions of the first ATI peak and the Freeman resonance at 4.4×10^{13} W/cm^2 are the same, so the angular momentum of the second ATI peak exhibits the PAD structure as expected.

Furthermore, based on nonperturbative scattering theory, Guo *et al.* [8] established a rule to predict the jet number of each order ATI peak for multiphoton ionization, which is twice the number of the maxima of generalized phased Bessel functions in a certain domain. The results predicted by the scattering theory and the experimental results are given in Table I. Except for the numbers of the first and second ATI peaks, the predicted results agree well with the experimental data. The phenomenon that three more jets may appear with one-more-photon absorption, predicted by the scattering theory, is not observed in our experiment. For the first and second ATI peaks, the jet numbers calculated from the theoretical results are different from the experimental data. This may be caused by the influence of the transient resonant

TABLE I. Comparison of the experimental jet number of each ATI peak at three intensities with theoretical results.

| Intensity | ATI order | | | |
	First	Second	Third	Fourth
	Experimental results			
1.8×10^{13} W/cm^2	3	4	5	6
3.1×10^{13} W/cm^2	4	5	6	7
4.4×10^{13} W/cm^2	4	5	6	7
	Theoretical results			
1.8×10^{13} W/cm^2	1	2	5	6
3.1×10^{13} W/cm^2	0	5	6	7
4.1×10^{13} W/cm^2	2	3	6	7

states. For example, the $5g$ state is shifted into resonance at 3.1×10^{13} W/cm^2 due to the ac Stark effect; thus the PADs of the first ATI peak will exhibit $l = 5$ (four jets), while no jets are predicted by the scattering theory without the resonant effect. A more comprehensive theory about the PADs of each order ATI peak considering the influence of the transient resonant states is required.

IV. CONCLUSION

In summary, we have studied the two-dimensional momentum distributions and energy-angular distributions of photoelectrons obtained by COLTRIMS. We have measured the PADs of nonresonant ionization, Freeman resonance, and each order ATI peak. The angular momentum of near-threshold photoelectrons predicted by semiclassical theory is in complete accordance with that of our experiment. Two pronounced intensity-dependent features are observed in the low-energy photoelectrons: (i) two sets of photoelectrons fanning out radially from the origin with different angular distributions are present at low intensity—the one with higher energy may result from the ac Stark splitting via one-photon coupling between the $5d$ and $4f$ states; and (ii) the splitting effect of the Freeman resonance at high intensity, which may originate from channel switching simultaneously from the resonant $5g$ and $6g$ states. We observe that the channel of nine-photon resonant ionization has switched to a ten-photon process but the nine-photon nonresonance may remain at the intensity of 3.1×10^{13} W/cm^2. We have confirmed the selection rule that the dominant angular momentum steps up one by one with increasing the ATI order. Compared with the nonperturbative scattering theory, our experimental results reveal that the transient resonant states induced by the ac Stark effect may significantly affect the PADs on the first- and second-order ATI peaks.

[1] P. Agostini, F. Fabre, G. Mainfray, G. Petite, and N. K. Rahman, Phys. Rev. Lett. **42**, 1127 (1979).

[2] J. H. Eberly, J. Javanainen, and K. Rzewski, Phys. Rep. **204**, 331 (1991).

[3] G. G. Paulus, W. Nicklich, H. Xu, P. Lambropoulos, and H. Walther, Phys. Rev. Lett. **72**, 2851 (1994).

[4] D. A. Telnov and Shih-I Chu, Phys. Rev. A **83**, 063406 (2011).

[5] R. R. Freeman, P. H. Bucksbaum, H. Milchberg, S. Darack, D. Schumacher, and M. E. Geusic, Phys. Rev. Lett. **59**, 1092 (1987).

[6] B. Yang, K. J. Schafer, B. Walker, K. C. Kulander, P. Agostini, and L. F. DiMauro, Phys. Rev. Lett. **71**, 3770 (1993).

[7] M. J. Nandor, M. A. Walker, and L. D. Van Woerkom, J. Phys. B **31**, 4617 (1998).

[8] J. Zhang, W. Zhang, Z. Xu, X. Li, P. Fu, D.-S. Guo, and R. R. Freeman, J. Phys. B **35**, 4809 (2002); D.-S. Guo, J. Zhang, Z. Xu, X. Li, P. Fu, and R. R. Freeman, Phys. Rev. A **68**, 043404 (2003); L. Bai, J. Zhang, Z. Xu, and D.-S. Guo, Phys. Rev. Lett. **97**, 193002 (2006).

[9] Z. Chen, T. Morishita, A.-T. Le, M. Wickenhauser, X. M. Tong, and C. D. Lin, Phys. Rev. A **74**, 053405 (2006).

[10] A. Rudenko, K. Zrost, C. D. Schröter, V. L. B. de Jesus, B. Feuerstein, R. Moshammer, and J. Ullrich, J. Phys. B **37**, L407 (2004).

[11] C. M. Maharjan, A. S. Alnaser, I. Litvinyuk, P. Ranitovic, and C. L. Cocke, J. Phys. B **39**, 1955 (2006).

[12] D. G. Arbó, K. I. Dimitriou, E. Persson, and J. Burgdorfer, Phys. Rev. A **78**, 013406 (2008).

[13] T. Marchenko, H. G. Muller, K. J. Schafer, and M. J. J. Vrakking, J. Phys. B **43**, 095601 (2010).

[14] T. Marchenko, H. G. Muller, K. J. Schafer, and M. J. J. Vrakking, J. Phys. B **43**, 185001 (2010).

[15] J. Ullrich, R. Moshammer, A. Dorn, R. Dorner, L. P. H. Schmidt, and H. Schmidt-Bocking, Rep. Prog. Phys. **66**, 1463 (2003).

[16] Y. Liu, X. Liu, Y. Deng, C. Wu, H. Jiang, and Q. Gong, Phys. Rev. Lett. **106**, 073004 (2011); X. Liu, C. Wu, Z. Wu, Y. Liu, Y. Deng, and Q. Gong, Phys. Rev. A **83**, 035403 (2011); X. Liu *et al.*, J. Opt. Soc. Am. B **28**, 293 (2011).

[17] P. B. Corkum, Phys. Rev. Lett. **71**, 1994 (1993); J. L. Krause, K. J. Schafer, and K. C. Kulander, *ibid.* **68**, 3535 (1992); V. L. B. de Jesus *et al.*, J. Phys. B **37**, L161 (2004).

[18] D. G. Arbó, S. Yoshida, E. Persson, K. I. Dimitriou, and J. Burgdorfer, Phys. Rev. Lett. **96**, 143003 (2006).

[19] [http://physics.nist.gov/cgi-bin/ASD/energy1.pl].

[20] M. Schuricke, G. Zhu, J. Steinmann, K. Simeonidis, I. Ivanov, A. Kheifets, A. N. Grum-Grzhimailo, K. Bartschat, A. Dorn, and J. Ullrich, Phys. Rev. A **83**, 023413 (2011).

[21] R. Wiehle, B. Witzel, H. Helm, and E. Cormier, Phys. Rev. A **67**, 063405 (2003).

[22] V. Schyja, T. Lang, and H. Helm, Phys. Rev. A **57**, 3692 (1998).

[23] Y. Deng, Y. Liu, X. Liu, H. Liu, Y. Yang, C. Wu, and Q. Gong, Phys. Rev. A **84**, 065405 (2011).

[24] P. Hansch, M. A. Walker, and L. D. Van Woerkom, Phys. Rev. A **57**, R709 (1998).